Engineering Fracture Mechanics 276 (2022) 108887

Contents lists available at ScienceDirect

Engineering Fracture Mechanics

journal homepage: www.elsevier.com/locate/engfracmech

Modeling of projectile penetrating fiber-reinforced concrete via the continuum discontinuum element method

Bowen Sun [a], Fei Han [a,*], Chun Feng [b], Yong Mei [c,*], Yunhou Sun [c], Jun Shen [c], Ao Zhang [c]

[a] State Key Laboratory of Structural Analysis for Industrial Equipment, Department of Engineering Mechanics, International Research Center for Computational Mechanics, Dalian University of Technology, Dalian 116023, China
[b] Key Laboratory for Mechanics in Fluid Solid Coupling Systems, Institute of Mechanics, Chinese Academy of Sciences, Beijing 100190, China
[c] Institute of Defense Engineering, AMS, Beijing 100036, China

ARTICLE INFO

Keywords:
CDEM
Fiber-reinforced concrete
Penetration
Crack width
Weibull distribution

ABSTRACT

In this paper, the projectile penetrating fiber-reinforced concrete (FRC) is modeled and simulated by the continuum discontinuum element method (CDEM) and a fiber-block interpolation coupling algorithm. The Mohr–Coulomb constitutive model is applied to the blocks to calculate the block forces, and the Mohr–Coulomb criterion and the maximum tensile criterion are applied to estimate the failure of contact surfaces. Numerical simulations of projectiles penetrating plain concrete and FRC with 1 to 3 vol% are performed. We verify the validity of the model by predicting the crack morphology and penetration depth for plain concrete and FRC, which are in agreement with experimental results. Detailed images of crack surfaces in the concrete blocks caused by projectile penetration are included. The effects of fiber content on crack width are analyzed. The results indicate that the normalized widths of the cracks approximately satisfy the Weibull distribution. Compared with plain concrete, the addition of fibers results in a reduction in both the expectation and variance of crack widths. However, the degree of reduction weakens as fiber content increased.

1. Introduction

Concrete is an important multifunctional composite material composed of aggregates, mortar, and interfacial transition zones (ITZ). It is mainly used to withstand compression because of its excellent compressive performance. However, the tensile performance of concrete is comparatively weak. Therefore, improving the tensile performance of concrete to achieve a better overall performance is a highly relevant research area. One way to achieve this is through a mixture called fiber-reinforced concrete (FRC) [1,2], which is obtained by combining concrete with short and discrete fibers. FRC generally possesses better tensile and shear strength than plain concrete. At present, a variety of fibers have been used to prepare FRC, such as steel fibers [3], carbon fibers [4], and glass fibers [5]. Steel fibers have the most extensive applications owing to their lower cost and relatively good performance.

Numerous tests have proven that, under various loading conditions, the initiation and propagation of local cracks can be effectively inhibited by adding fibers to concrete [6]. Thus, FRC maintains its integrity more easily and exhibits better mechanical properties than plain concrete. The role of fibers in inhibiting the initiation and propagation of cracks can be explained by their bridging effect of fibers [7]; fibers occupy the space around the aggregates and connect the ITZ with the mortars by forming a spatial web-like structure, which hinders the widening of micro-cracks in the ITZ and its propagation to mortars. Stress transfer is

* Corresponding authors.
E-mail addresses: hanfei@dlut.edu.cn (F. Han), meiyong1990@126.com (Y. Mei).

https://doi.org/10.1016/j.engfracmech.2022.108887
Received 18 May 2022; Received in revised form 9 October 2022; Accepted 13 October 2022
Available online 23 October 2022

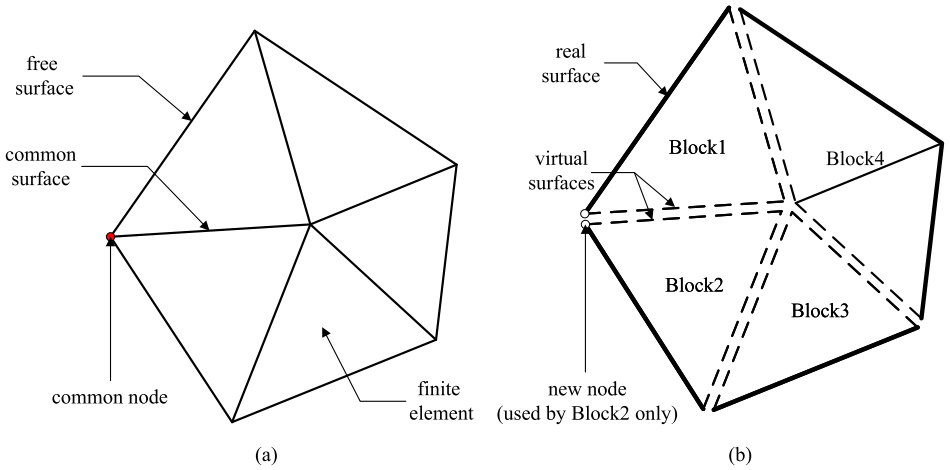

Fig. 1. (a) Geometric model of a continuum, (b) blocks and surfaces.

also improved by fibers bridging cracked sections, and therefore the mechanical properties of FRC after cracking are enhanced [8–10]. Fiber content also has a significant effect on the static and dynamic mechanical properties of FRC, for example, the tensile strength of FRC increases with fiber content [11,12]. FRC is regarded as a favorable shelter material against extreme loadings such as explosions and impacts because it is difficult to generate cracks in FRC. Numerous penetration tests have been conducted to study the response of FRC under impact loading and most of them focused mainly on the effect of fibers on the failure mode of FRC [13–15]. O'Neil et al. [13] and Anderson et al. [14] reported that fiber content has little effect on the penetration depth of FRC, whereas the incorporation of fibers contributes to arresting the propagation of cracks, thus leading to craters of smaller volume. Máca et al. [15] indicated that the increase of fiber content has no significant effect on crater dimension when the content is larger than 2%. However, researches on the effect of fiber on the crack width are scarce. Moreover, these researches only include analysis of the maximum crack width on the impacted surface. For example, Wu et al. [16] studied the maximum crack width and the number of cracks on the impacted surface of polyvinyl alcohol fiber-reinforced concrete penetrated by projectiles.

Numerical simulations on FRC penetration have also been conducted. The methods most widely used are the finite element method [17], the discrete element method [18], and the smooth particle method [19]. In recent years, the continuum discontinuum element method (CDEM), which was applied in landslides [20] and hydraulic fracturing simulations [21,22], has also been gradually used to simulate dynamic problems such as penetration and explosion. For example, Feng et al. [23] simulated the entire process of penetration and blast of earth-penetrating weapons, and Wang et al. [24] described the fracture, fragmentation, and landing of a warhead after explosion.

In this study, we establish a model of the projectile penetrating FRC based on the CDEM. The process of projectile penetration into FRC is numerically simulated to investigate the effect of adding fibers on penetration-induced crack width.

The rest of this paper is organized as follows: Some basic concepts and the governing equations of the CDEM and its constitutive models adopted in this paper are introduced in Section 2. In Section 3, the parameters of the projectile, concrete, and fibers are provided, the geometric modeling method of the fibers is described, the crack surface and its associated parameters are defined, and a semi-discrete fiber-block coupling method, which is adopted in FRC modeling, is described. The numerical results of the projectile penetrating blocks, including plain concrete and FRC with 1 vol% and 3 vol% steel fibers, are analyzed and compared in Section 4. Finally, Section 5 presents a summary of the study.

2. The continuum discontinuum element method

The CDEM is a dynamic explicit numerical method that uses separable elements for the Lagrangian system. In this method, the dynamic relaxation algorithm is used to obtain an explicit iterative solution [25].

2.1. Blocks and contact surfaces

The geometric model of a continuum can be discretized with finite elements, where adjacent elements share common nodes and surfaces, as shown in Fig. 1(a). By inserting new nodes to separate the original common surfaces, the geometric model can be divided into several blocks, each consisting of one or more finite elements. As shown in Fig. 1(b), a pentagonal continuum is divided into four blocks, of which the block 4 consists of two elements and the others all consisting of one element.

In this study, we define two types of contact surfaces. One is the two new surfaces formed by inserting new nodes into a common surface between elements, called the virtual surfaces. The other is the external surfaces of the geometric model, called the real surfaces. Both types of surface are collectively referred to as contact surfaces.

The forces between the blocks is transmitted by introducing a semi-spring model on the contact surfaces [26]. The semi-spring model also contains two modes corresponding to the cases of virtual and real surfaces, respectively. Between two corresponding

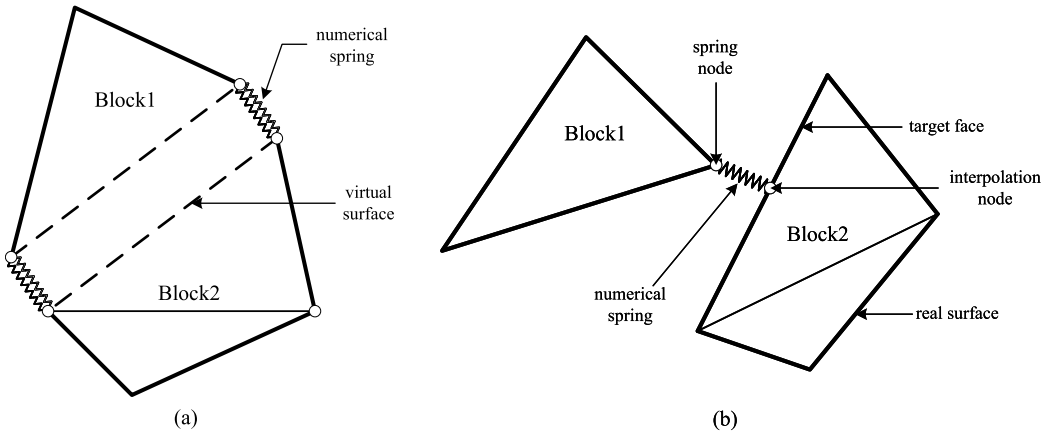

Fig. 2. The semi-spring model on contact surfaces: (a) virtual surface, (b) real surface.

virtual surfaces, each node is connected by two "springs" in parallel, as shown in Fig. 2(a). The transmission of forces is calculated through the deformation of the "springs". When the spring force exceeds the maximum load that the spring can carry, the spring will break and remain unable to longer transmit forces. When all springs on a virtual surface break, the virtual surface transforms into a real surface, which means that a local fracture occurs in the continuum from the perspective of the whole continuum. The semi-spring model between the real surfaces of two blocks is often used to describe the contact between the blocks as shown in Fig. 2(b). The vertex of block 1 is a spring node and a face on block 2 is used as a target face when the distance between the spring node and the face is less than a searching tolerance. By using the normal direction of the target face as its own normal direction, the spring finds an interpolation node on the target face to describe the contact behavior.

2.2. Governing equation

The governing equation of the CDEM is established based on the Lagrangian energy system [27]

$$\frac{\partial}{dt}(\frac{\partial L}{\partial \dot{u}}) - \frac{\partial L}{\partial u} = Q, \tag{1}$$

where Q is the conservative force of the system, L is the Lagrangian function, which can be written as

$$L = \Pi_m + \Pi_e + \Pi_f, \tag{2}$$

where Π_m, Π_e, and Π_f are the kinetic, elastic, and potential energies of the system, respectively.

In the CDEM, the energy of an element is written as

$$L = \int_V \frac{1}{2}\rho \dot{u}^2 dV + \int_V \frac{1}{2}\sigma\varepsilon dV - \int_V f u dV, \tag{3}$$

where ρ is the density, u is the displacement, $\dot{u}$ is the velocity, σ is the stress tensor, ε is the strain tensor, f is the body force applied to the element and V is the volume of the element.

The non-conservative force Q on the element includes the damping force Q_μ and the external boundary force Q_T, which can be written as

$$Q_\mu = \int_V \mu \dot{u} dV, \qquad Q_T = -\int_S T dS, \tag{4}$$

where μ is the damping coefficient and T is the boundary traction. By treating u and $\dot{u}$ as two independent values, and substituting Eqs. (3) and (4) into Eq. (1), we get

$$\int_V \rho \ddot{u} dV - \int_V \mu \dot{u} dV - \frac{\partial}{\partial u}\int_V \frac{1}{2}\sigma\varepsilon dV = -(\int_V f dV + \int_S \overline{T} dS). \tag{5}$$

Based on Eq. (5) and introducing the displacement, velocity and acceleration of the element nodes, the discrete form of the element equilibrium equation can be written as

$$\boldsymbol{M}\ddot{\boldsymbol{u}} + \boldsymbol{C}\dot{\boldsymbol{u}} + \boldsymbol{K}\boldsymbol{u} = \boldsymbol{F}, \tag{6}$$

where $\ddot{\boldsymbol{u}}$, $\dot{\boldsymbol{u}}$, and $\boldsymbol{u}$ are the acceleration, velocity, and displacement of the nodes in the element, respectively; and $\boldsymbol{M}$, $\boldsymbol{C}$, $\boldsymbol{K}$ are the mass matrix, damping matrix, and stiffness matrix of the element, respectively. $\boldsymbol{F}$ is the external loading vector.

2.3. Calculation of block forces

Incremental form of block constitutive model

The stress increment of an element at the current time step $\Delta\sigma_{ij}(t)$ is written as

$$\Delta\sigma_{ij}(t) = 2G\Delta\varepsilon_{ij}(t) + (K - \frac{2}{3}G)\Delta\theta(t)\delta_{ij}, \tag{7}$$

where G and K are the shear and bulk modulus of the element, respectively; $\Delta\varepsilon_{ij}(t)$ and $\Delta\theta(t)$, which can be obtained from the increment of node displacements at the current time step, are the strain and bulk strain increment of the element at the current time step, respectively and δ_{ij} is the Kronecker symbol.

Failure criterion

The failure criterion of the elements is established using the Mohr–Coulomb criterion and the maximum tensile criterion. First, three constants N_φ, α_P, and σ_P are defined as

$$\begin{cases} N_\varphi = \frac{1+\sin\varphi}{1-\sin\varphi}, \\ \alpha_P = \sqrt{1+N_\varphi^2} + N_\varphi, \\ \sigma_P = T(t)N_\varphi - 2C(t)\sqrt{N_\varphi}, \end{cases} \tag{8}$$

where $C(t)$ and $T(t)$ are the cohesion and tensile strength of the element at the current time step, respectively, and φ is the friction angle of the element.

Based on the stress increment of the element at the current time step obtained using Eq. (7) and the element's stress at the previous time step, the trial stress of the element at the current time step, $\sigma'_{ij}(t)$, can be written as

$$\sigma'_{ij}(t) = \sigma_{ij}(t-\Delta t) + \Delta\sigma_{ij}(t). \tag{9}$$

The trial principal stresses $\sigma'_1(t)$, $\sigma'_2(t)$, and $\sigma'_3(t)$ (sorted from largest to smallest) are calculated based on $\sigma'_{ij}(t)$. Then, some indices can be calculated to determine whether the plasticity has occurred:

$$\begin{cases} f_s = \sigma'_1(t) - \sigma'_3(t)N_\varphi + 2C(t)\sqrt{N_\varphi}, \\ f_t = \sigma'_3(t) - T(t), \\ h = f_t + \alpha_P[\sigma'_1(t) - \sigma_P], \end{cases} \tag{10}$$

where f_s and f_t are the shear and tensile plastic deformation indices, respectively, and h is an index that determines the current stress zone of the element. If $f_s \geqslant 0$ and $h \leqslant 0$, the element undergoes shear plastic deformation; if $f_t \geqslant 0$ and $h \geqslant 0$, the element undergoes tensile plastic deformation; otherwise, the element does not undergo a plastic deformation.

Modification of element stress

First, four constants, λ^s, α_1, α_2 and N_ψ are defined. They can be written as

$$\begin{cases} \lambda^s = \frac{f_s}{(\alpha_1-\alpha_2 N_\psi)-(-\alpha_1 N_\psi+\alpha_2)N_\psi}, \\ \alpha_1 = K + \frac{4}{3}G, \\ \alpha_2 = K - \frac{2}{3}G, \\ N_\psi = \frac{1+\sin\psi}{1-\sin\psi}, \end{cases} \tag{11}$$

where ψ is the dilation angle of the element.

If the element undergoes shear plastic deformation, the trial principal stress is modified as follows

$$\begin{cases} \sigma_1(t) = \sigma'_1(t) - \lambda^s(\alpha_1 - \alpha_2 N_\psi), \\ \sigma_2(t) = \sigma'_2(t) - \lambda^s\alpha_2(1 - N_\psi), \\ \sigma_3(t) = \sigma'_3(t) - \lambda^s(-\alpha_1 N_\psi + \alpha_2). \end{cases} \tag{12}$$

If the element undergoes tensile plastic deformation, the trial principal stress is modified as follows

$$\begin{cases} \sigma_1(t) = \sigma'_1(t) - \left[\sigma'_3(t) - T(t)\right]\frac{\alpha_2}{\alpha_1}, \\ \sigma_2(t) = \sigma'_2(t) - \left[\sigma'_3(t) - T(t)\right]\frac{\alpha_2}{\alpha_1}, \\ \sigma_3(t) = T(t). \end{cases} \tag{13}$$

If no plastic deformation occurs, the trial principal stress is the principal stress of the element at the current time step.

Subsequently, the modified principal stress is converted to the global coordinate system to obtain the stress tensor $\sigma_{ij}(t)$ of the element at the current time step, and then the nodal forces contributed by the element stress are calculated.

Modification of cohesion and tensile strength

The cohesion and tensile strength of the element decrease with the plastic deformation. The effective plastic shear strain and effective plastic bulk strain of the element are calculated using the nodal displacement at the current time step to obtain the cohesion and tensile strength of the element at the next time step, which can be written as

$$\begin{cases} C(t+\Delta t) = C_0(1-\frac{\gamma_p(t)}{\gamma_f}), \\ T(t+\Delta t) = T_0(1-\frac{\varepsilon_p(t)}{\varepsilon_f}), \end{cases} \tag{14}$$

where C_0 and T_0 are the cohesion and tensile strength of the element at the initial time step, respectively; γ_f and ε_f are the shear fracture strain and volume tensile fracture strain of the element, respectively; and $\gamma_p(t)$ and $\varepsilon_p(t)$ are the effective plastic shear strain and effective plastic bulk strain of the element at the current time step, respectively.

2.4. Calculation of contact forces

Constitutive model of contact surfaces

The difference between the displacement increments of the spring node and the interpolation node is used as the increment of the spring deformation. Thus the normal and tangent contact forces can be written as [26]

$$\begin{cases} \hat{F}_n(t+\Delta t) = \hat{F}_n(t) - \hat{K}_n \Delta \hat{d}_n(t), \\ \hat{F}_s(t+\Delta t) = \hat{F}_s(t) - \hat{K}_s \Delta \hat{d}_s(t), \end{cases} \tag{15}$$

where $\hat{F}_n(t)$ and $\hat{F}_s(t)$ are the normal and tangent contact forces of the spring at the current time step, respectively; $\hat{K}_n$ and $\hat{K}_s$ are the normal and tangent contact stiffnesses of the spring, respectively; and $\hat{\Delta}d_n$ and $\hat{\Delta}d_s$ are the normal and tangent increments of the spring deformation, respectively.

Failure criterion and modification of spring forces

The failure criterion of the contact surfaces is established using the Mohr–Coulomb criterion and the maximum tensile criterion. This failure criterion can be written as [26]

$$\begin{cases} (1)If \quad -\hat{F}_n(t) \geqslant \hat{T}(t)\cdot\hat{A}, \\ \hat{F}_n(t) = \hat{F}_s(t) = 0, \\ next\ step \quad \hat{C}(t+\Delta t) = 0, \hat{T}(t+\Delta t) = 0, \\ (2)If \quad \hat{F}_s(t) \geqslant \hat{F}_n(t)\tan\hat{\varphi} + \hat{C}(t)\cdot\hat{A}, \\ \hat{F}_s(t) = \hat{F}_n(t)\tan\hat{\varphi} + \hat{C}(t)\cdot\hat{A}, \\ next\ step \quad \hat{C}(t+\Delta t) = 0, \hat{T}(t+\Delta t) = 0, \end{cases} \tag{16}$$

where $\hat{T}(t)$, $\hat{C}(t)$ and $\hat{\varphi}$ are the tensile strength, cohesion and the friction angle of the spring at the current time step, respectively; and $\hat{A}$ is the contact area of the spring.

Then, the modified spring forces are assigned to the element nodes to obtain the nodal forces contributed by the contact forces.

2.5. Flowchart of algorithm

In this study, the dynamic relaxation method is used to solve Eq. (6) explicitly. The flowchart of the algorithm is shown in Fig. 3. The nodal acceleration $\ddot{u}(t)$ at the current time step is obtained from the nodal velocity $\dot{u}(t-\Delta t)$ and the nodal displacement $u(t-\Delta t)$ at the previous time step.

$$\ddot{\boldsymbol{u}}(t) = \boldsymbol{M}^{-1}[\boldsymbol{F}(t-\Delta t) - \boldsymbol{C}\dot{\boldsymbol{u}}(t-\Delta t) - \boldsymbol{K}\boldsymbol{u}(t-\Delta t)]. \tag{17}$$

Note that the nodal forces contributed by the contact surfaces are included in the external force $\boldsymbol{F}(t-\Delta t)$. The damping matrix $\boldsymbol{C}$ can be written as [28]

$$\boldsymbol{C} = \alpha\boldsymbol{M} + \beta\boldsymbol{K}, \tag{18}$$

where α and β are the mass damping coefficients and stiffness damping coefficient, respectively. In this study, $\alpha = 0$ and $\beta = 2\times10^{-7}$.

Then the nodal velocity and nodal displacement at the current time step can then be written as

$$\begin{cases} \dot{\boldsymbol{u}}(t) = \dot{\boldsymbol{u}}(t-\Delta t) + \ddot{\boldsymbol{u}}(t)\Delta t, \\ \boldsymbol{u}(t) = \boldsymbol{u}(t-\Delta t) + \dot{\boldsymbol{u}}(t)\Delta t. \end{cases} \tag{19}$$

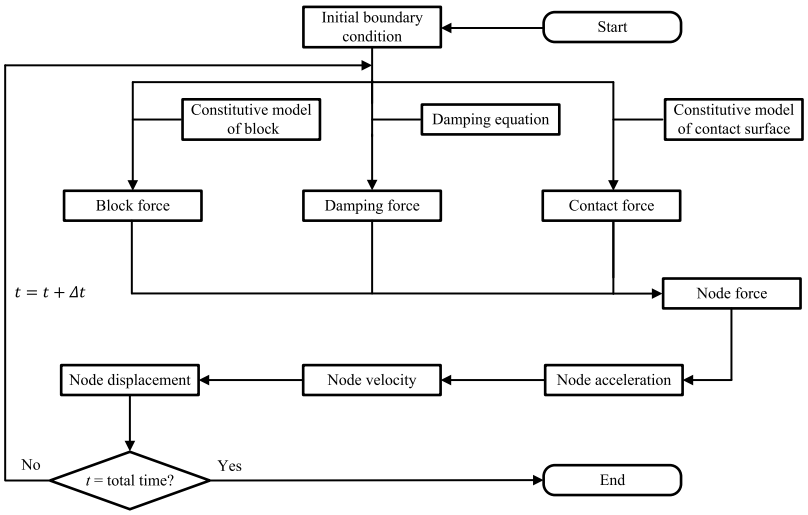

Fig. 3. Calculation flowchart of the CDEM.

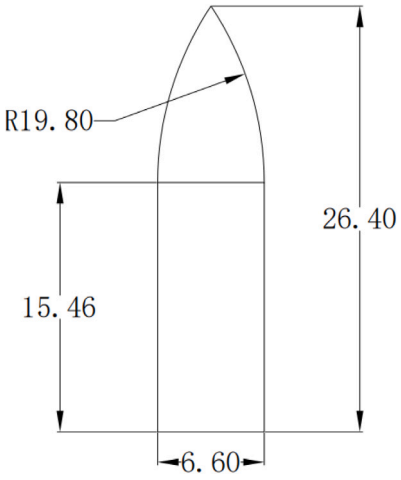

Fig. 4. Dimension of the projectile (unit: mm).

3. Geometric models, material parameters, and correlation algorithm

3.1. Projectile and concrete target

The dimensions of the projectile are shown in Fig. 4, and its material is 30CrMnSiA, which satisfies the linear elasticity here. Relevant material parameters of the projectile are shown in Table 1. The initial velocity of the projectile is 1080 m/s.

The dimensions of the concrete target are 300 mm × 300 mm × 300 mm, and the Mohr–Coulomb model and the maximum tensile stress model are used (see Section 2.3 for details). Relevant material parameters of the target are also listed in Table 1. The geometric parameters, as well as some of the material parameters, of the projectile and concrete block are referenced from our previous work [29], and the cohesion of the concrete is

$$C = \frac{\sigma_c}{2tan(45 + \varphi/2)}, \tag{20}$$

where σ_c and φ are the compression strength and friction angle of the concrete, respectively.

To reduce computational costs, a quarter of the total geometry is isolated for modeling, and the mesh is subdivided around the impact point. The model (including the projectile) is divided into four-node tetrahedral elements, as shown in Fig. 5, for a total of 3686 nodes and 15 206 elements.

All element surfaces in the concrete target are treated as contact surfaces and the constitutive model is described in Section 2.4. The normal and tangent contact stiffnesses $\hat{K}_n$ and $\hat{K}_s$ of the contact surfaces are inherited from the concrete elements.

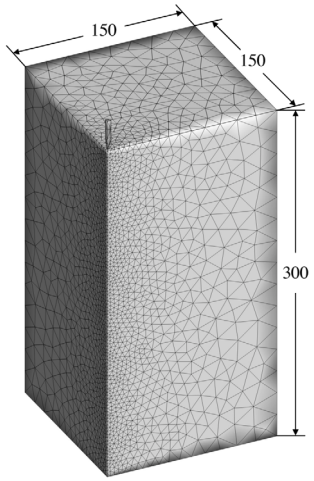

Fig. 5. A quarter of geometric model and the tetrahedral elements (unit: mm).

Table 1
Parameters of projectile and concrete.

Parameter	Unit	Projectile	Concrete
Density	g/m^3	7850	2500
Young's modulus	GPa	196	33.1
Possion's ratio	–	0.3	0.2
Cohesion	MPa	–	12.1
Tensile strength	MPa	1080	1.0
Compression strength	MPa	1080	51.9
Friction angle	°	0	40
Dilation angle	°	0	10

3.2. Crack surface and crack width

The condition for fracture at a contact surface is that all springs on the virtual surface have failed, i.e., the springs are no longer used to calculate the forces, but are still used to calculate the deformation. The two corresponding virtual surfaces on which the springs have completely failed are called crack surfaces, and the width of each crack surface d is defined as

$$d = \frac{1}{2n}\sum_{i=1}^{2n}\hat{d}_i, \tag{21}$$

where n is the number of nodes on each crack surface ($n = 3$ for four-node tetrahedral elements) and $\hat{d}_i$ is the deformation of the ith ($i = 1, 2, \ldots, 2n$) spring.

3.3. Random short fibers

In this study, short and discrete fibers are modeled in the concrete. The parameters listed in Table 2 are used to model these fibers. According to data of pullout test in [12], the cohesion and axial stiffness are determined by bond strength and the ratio of the bond strength to pullout slip, respectively. To generate discrete short fibers more efficiently, the following simplification is adopted based on the fact that the diameter of a fiber is much smaller than the size of the concrete: each fiber is considered as a line segment in space and the volume occupied by the intersecting part is ignored. We employed the following method from our previous work [30] to generate random fibers consisting of n line segments with length l:

(1) Within the volume Ω occupied by the concrete, a seed is randomly generated as the starting point of a fiber based on a uniform distribution. The angles between the fiber axis and the positive direction of the x and z axes satisfy a uniform distribution in $[0, 2\pi]$;

(2) Generate a node at a distance l from the starting point along the direction of the fiber axis. Subsequent nodes are generated in the same way; if any generated node falls outside Ω, then we delete all nodes of this fiber from the starting point and return to step 1 until $n + 1$ nodes are generated. These $n + 1$ nodes are sequentially connected to form n line segments, which constitute a fiber.

(3) step (2) is repeated until all fibers are generated (the number of fibers is determined by the geometric parameters and volume fraction of the fibers).

Fig. 6 shows concrete with 1 vol% fiber content.

Table 2
Parameters of fiber.

Parameter	Unit	Value
Diameter	mm	0.5
Length	mm	20
Young's modulus	GPa	100
Density	g/m^3	7800
Possion's ratio	–	0.25
Tensile strength	MPa	808
Cohesion	MPa	10
Axial stiffness	Pa/m	2×10^{10}

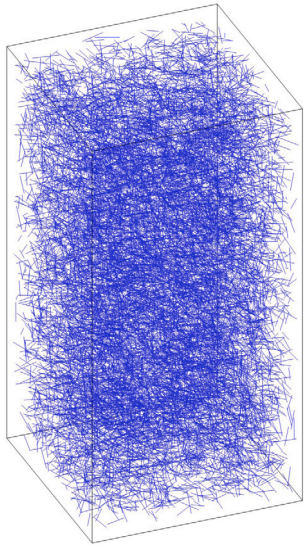

Fig. 6. Schematic diagram of discrete fibers.

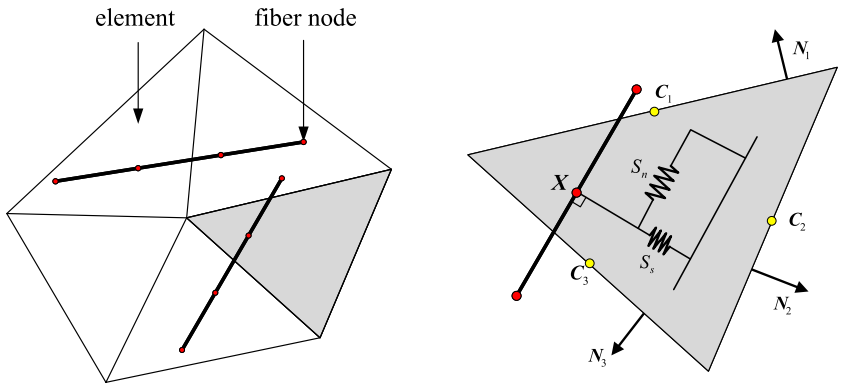

Fig. 7. Schematic diagram of fiber-block correlation algorithm: the right subfigure is a local refinement of the left subfigure.

3.4. Fiber-block correlation algorithm

To study the influence of fibers on the penetration, the fibers are treated as rod elements and the correlation between fibers with the block is calculated by means of insertion. A schematic diagram of the correlation algorithm is shown in Fig. 7.

Determination of insertion element

First, we find a fiber node and its corresponding insertion element, that is, the element in which the fiber node is located. Taking the triangular element shown in Fig. 7 as an example, the insertion element needs to satisfy the following conditions:

$$\begin{cases} J_i = \frac{\boldsymbol{C}_i - \boldsymbol{X}}{|\boldsymbol{C}_i - \boldsymbol{X}|} \cdot \boldsymbol{N}_i, \\ J_i \geqslant 0, \ \forall \ i = 1, 2, \ldots, n \ , \end{cases} \tag{22}$$

where $\boldsymbol{X}$ is the position vector of the fiber node and $\boldsymbol{C}_i$ and $\boldsymbol{N}_i$ are the position vector and external normal unit vector of the midpoint of the ith edge (with $n = 3$ edges for a triangular element), respectively.

Calculation of spring forces

The correlation between a fiber node and an element is established by introducing springs $\mathbb{S}_n$ and $\mathbb{S}_s$ at the fiber node. The spring $\mathbb{S}_n$ along the fiber axial direction is used to describe the pullout behavior, and the spring $\mathbb{S}_s$ perpendicular to the fiber axial direction is used to describe the extrusion behavior. At the current time step, the displacement increment of the fiber node along the fiber axis, $\Delta\bar{u}_n(t)$, and the displacement increment of the fiber node perpendicular to the fiber axis, $\Delta\bar{u}_s(t)$, are obtained by solving Eq. (6). Subsequently, the deformation increments of $\mathbb{S}_n$ and $\mathbb{S}_s$, $\Delta\bar{d}_n(t)$ and $\Delta\bar{d}_s(t)$, are obtained as follows:

$$\begin{cases} \Delta\bar{d}_n(t) = \Delta\bar{u}_n(t) - \sum_{i=1}^{n} w^i \Delta u_n^i(t), \\ \Delta\bar{d}_s(t) = \Delta\bar{u}_s(t) - \sum_{i=1}^{n} w^i \Delta u_s^i(t), \end{cases} \tag{23}$$

where $\Delta u_n^i(t)$ and $\Delta u_s^i(t)$ are the displacement increment components of the ith node of the insertion element along and perpendicular to the fiber axis at the current time step, respectively, and w_i is the weighting coefficient of the ith node of the insertion element.

The axial and lateral forces at the next time step are calculated from the deformation increments of $\mathbb{S}_n$ and $\mathbb{S}_s$ at the current time step and can be written as

$$\begin{cases} \bar{F}_n(t + \Delta t) = \bar{F}_n(t) - \bar{K}_n \Delta\bar{d}_n(t), \\ \bar{F}_s(t + \Delta t) = \bar{F}_s(t) - \bar{K}_s \Delta\bar{d}_s(t), \end{cases} \tag{24}$$

where $\bar{F}_n$ and $\bar{K}_n$ are the axial force and axial stiffness of $\mathbb{S}_s$, respectively, and $\bar{F}_s$ and $\bar{K}_s$ are the lateral force and lateral stiffness of $\mathbb{S}_s$, respectively.

Failure criterion and modification

The breakage and pullout failure of fibers are two failure modes considered. In this study, fiber breakage failure occurs when the elongation of a fiber is larger than a critical value, thus the two elements connected by the fiber no longer interact with each other. This failure is introduced briefly since it only occurs in some special cases when the cohesion between the fibers and the concrete is stronger than the tensile strength of the fibers, such as the crimped fibers and twin-cone fibers in ultra-high strength concrete [31]. For the straight fibers considered in this paper, the pullout failure is the primary failure mode since the cohesion is weaker than the tensile strength of the fibers. Therefore, a criterion that determines the pullout failure is introduced in detail.

A constant f_p is introduced to determine the pullout failure and can be written as

$$f_p = \bar{F}_n(t) - [\bar{C}(t) + \bar{\mu}\sigma_m(t)]\bar{A}, \tag{25}$$

where $\bar{C}(t)$ and $\bar{\mu}$ are the cohesion and friction coefficient between the fiber and the element at the current time step, respectively; $\sigma_m(t)$ is the bulk stress of the element node at the current time step; $\bar{A}$ is the common area between the fiber node and the element, which can be written as

$$\bar{A} = \pi \bar{D} \bar{L}, \tag{26}$$

where $\bar{D}$ is the diameter of the fiber and $\bar{L}$ is half of the sum of the lengths of the elements associated with the fiber node.

When $f_p \geqslant 0$, pullout failure occurs and $\bar{F}_n(t)$ and $\bar{C}(t)$ are modified to

$$\begin{cases} \bar{F}_n(t) = \bar{\mu}\sigma_m(t)\bar{A}, \\ \bar{C}(t) = 0. \end{cases} \tag{27}$$

When $f_p \leqslant 0$, the pullout failure does not occur and no modification is performed on $\bar{F}_n(t)$ and $\bar{C}(t)$.

Finally, the spring forces on $\mathbb{S}_n$ and $\mathbb{S}_s$ are assigned to the element nodes to obtain the nodal forces contributed by the fibers.

4. Results and discussion

4.1. Penetration experiment using a plain concrete target

An experiment [29] involving a projectile penetrating a plain concrete target perpendicularly is conducted. Relevant parameters are listed in Section 3.1. In this experiment, two orthogonal cracks and a tiny crack along the 45° direction are observed on the impacted surface, as shown in Fig. 8. The silicone casting method is used to reconstruct the trajectory of the projectile. The measured penetration depth is 169.03 mm, as shown in Fig. 9.

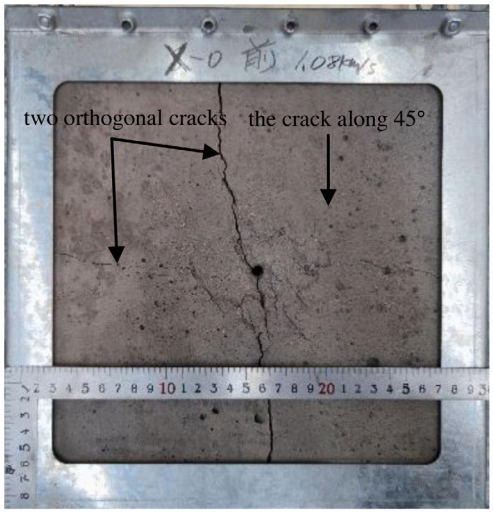

Fig. 8. Cracks on impacted surface.

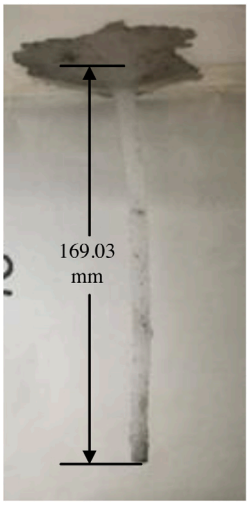

Fig. 9. The trajectory in the plain concrete target.

4.2. Penetration depth and cracks on the impacted surface

Simulation of the plain concrete

The numerical results using the proposed model show three main cracks on the impacted surface along the 0°, 45°, and 90° direction, respectively, as shown in Fig. 10. The morphology of the cracks obtained by the numerical simulation is consistent with the experimental observations.

In addition, we perform two similar numerical simulations by replacing the plain concrete in the above numerical example with 1 vol% and 3 vol% FRC (abbreviated as 1%FRC and 3%FRC respectively). All other numerical conditions remain unchanged. Fig. 11 shows their penetration depth–time curves. Whereas in which the magnitude of the penetration depth increases with time and the curves slowly tend to be horizontal. This phenomenon corresponds to the penetration process, in which the magnitude of the projectile's velocity gradually decreases and finally equals zero. The difference between the three curves is small when the time is less than 5×10^{-4}s, which indicates that the addition of fibers does not significantly enhance the resistance of concrete against the projectile during penetration. More specifically, the experimental data and numerical results for penetration depth of plain concrete are 169.03 mm and 169.24 mm, respectively, yielding a relative error of 0.12%. As for the 1%FRC and 3%FRC cases, the numerical results of penetration depth match those of plain concrete very closely. This implies that the addition of fibers has little effect on the penetration depth, and these predictions are consistent with the conclusions of [13,14].

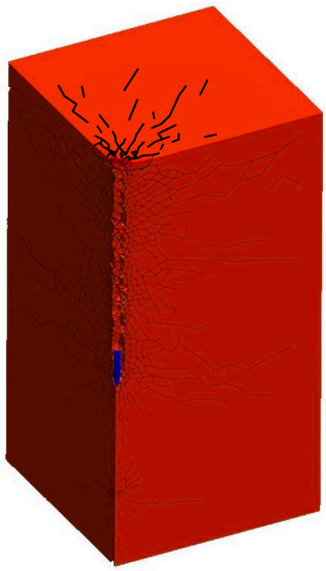

Fig. 10. Numerical result of plain concrete.

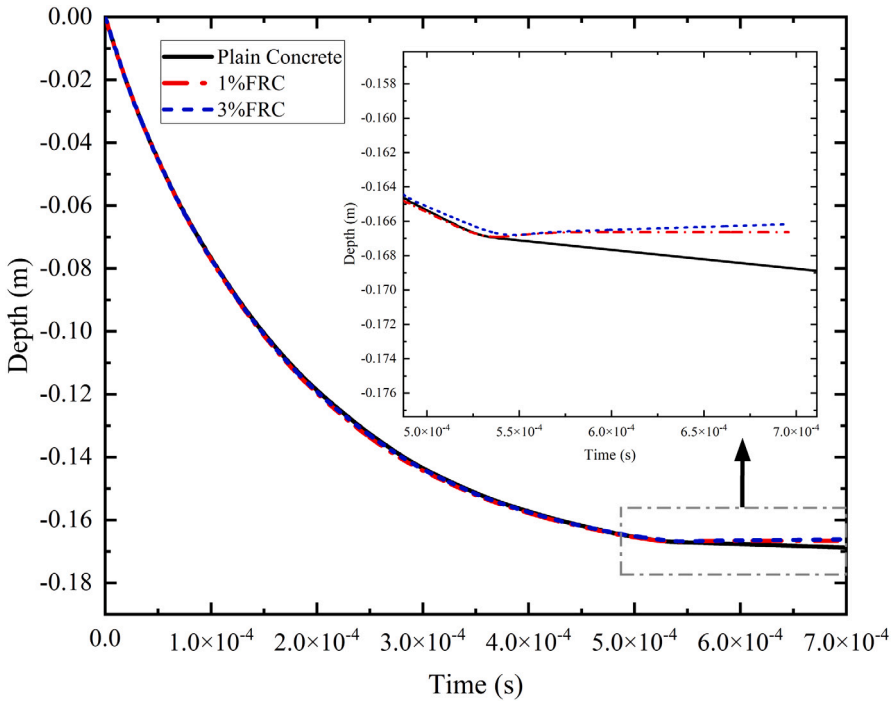

Fig. 11. Penetration depth–time curve of three kinds of concrete.

Simulation of the FRC

To further validate the correctness of the proposed model, we perform a numerical simulation for a penetration experiment [32]. The concrete target is a cylinder with radius 200 mm and projectile penetration velocity is 970 m/s. The same constitutive models in Section 3.1 are used in the simulation. The material parameters of the projectile and the concrete are listed in Table 3. The steel fiber content is 2%vol and the diameter and length of the fiber are 0.22 mm and 20 mm, respectively. The material parameters of the fibers are also listed in Table 3.

A quarter of the total model (including projectile) is divided into four-node tetrahedral elements for a total of 2243 nodes and 8556 elements. Fig. 12(a) is the experimental result of the crater and cracks on the impacted surface. Fig. 12(b) is the numerical result

Table 3
Parameters of concrete, projectile and fibers.

Parameter	Unit	Concrete	Projectile	Fibers
Young's modulus	GPa	40	196	200
Density	g/m^3	2500	7850	7850
Possion's ratio	–	0.2	0.3	0.3
Tensile strength	MPa	1.0	1080	1200
Compression strength	MPa	115.66	1080	1200
Cohesion	MPa	26.95	–	–
Axial stiffness	Pa/m	–	–	2×10^{10}

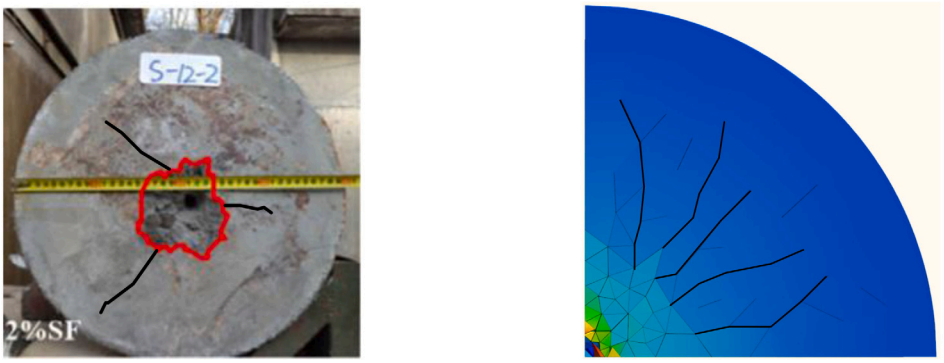

Fig. 12. Craters and cracks on impacted surface: (a) penetration experiment [32], (b) numerical simulation.

that shows several radial cracks on the impacted surface. These cracks do not extend to the lateral boundary of the target, which is consistent with the experimental observation. In addition, Fig. 13 shows the penetration depth–time curve. The experimental data and numerical result of penetration depth are 184 mm and 175 mm, respectively, yielding a relative error of −4.89%.

The penetration depth and the morphology of cracks obtained in all numerical simulations are consistent with the experimental results, which validates the correctness of the proposed method.

4.3. Crack surfaces

Large and continuous cracks, known as the main cracks, have the greatest influence on the mechanical properties of concrete. To study the influence of fiber content on the fracture of concrete, we define that the main crack surface of the concrete as the combination of all continuously distributed crack surfaces. This so-called continuous distribution refers to the existence of at least one common edge between any one crack surface contained in a main-crack surface and one or more other crack surfaces contained in the same main crack surface. Fig. 14 shows the main crack surfaces of three types of concrete introduced in Section 4.1. Each triangular patch in the subfigures represents a crack surface, and many patches are spliced at common edges to compose the main-crack surfaces. The color of the patches indicates the magnitude of the crack surface width d. From this figure, we can draw that the following conclusions:

(1) Overall, the number of patches in Fig. 14(a) is slightly greater than Fig. 14(b), and significantly higher than Fig. 14(c). That is, the number of crack surfaces in the plain concrete is slightly greater than that in the 1%FRC, and significantly more than that in the 3%FRC, which indicates that the addition of fibers can inhibit the propagation of cracks. This inhibitory effect can also be illustrated by comparing the areas of the main-crack surfaces (the total area of the patches in each subfigure): 0.3173 m^2 for plain concrete, 0.2897 m^2 for 1%FRC, and 0.2643 m^2 for 3%FRC. The areas of the main crack surfaces of 1%FRC and 3%FRC are 8.7% and 16.7% lower than that of plain concrete, respectively. Moreover, from Fig. 14(a) to (c), we can see that the color of the patches tends to be bluer with the increase of the fiber content. This indicates that the crack surface width decreases as the fiber content increases.

(2) From a local perspective, in Fig. 14(a–c), a crack surface zone with a lateral distribution (perpendicular to the direction of projectile's motion) is formed below the impacted surface. Each crack surface zone is comprised of many laterally distributed crack surfaces with relatively large widths. This means that the impact of the projectile tends to strip the impacted surface. As can be seen from Fig. 14, the width of these lateral crack surfaces gradually decreases with the increase of fiber content, which indicates that the addition of fibers can inhibit the stripping trend of the impact surface. It is worth mentioning that the fiber content also has effects on the size of crater. The displacement along penetrating direction at the last time step is presented, as shown in Fig. 15. A larger crater is shown in Fig. 15(a) and smaller craters of similar area are shown in Fig. 15(b) and (c), which is consistent with [15].

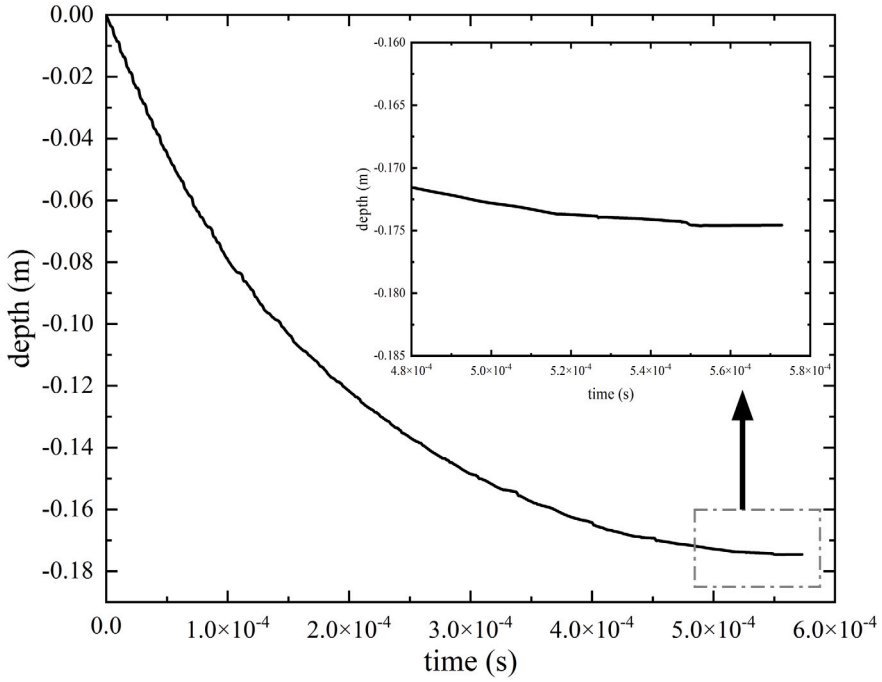

Fig. 13. Penetration depth–time curve.

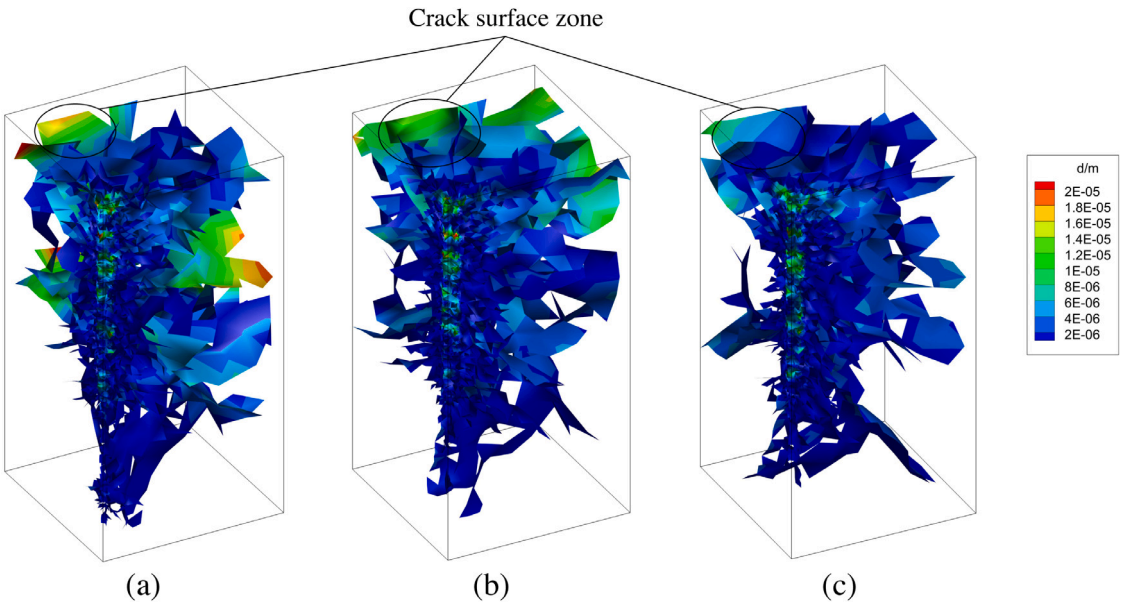

Fig. 14. Main crack surface: (a) plain concrete, (b) 1%FRC, (c) 3%FRC.

4.4. Statistics of normalized crack surface width

First, we define a value Δd as the minimum fineness to distinguish different crack surface widths. That is, the widths of two crack surfaces are considered to be identical when the absolute value of the width difference between the two crack surfaces is less than Δd. In this study, we set Δd equal to the displacement of the projectile within the last time step, which is the instant in which the projectile stops. However, because of the dynamic relaxation method used in the simulations, oscillations occur before the end of the penetration (when the velocity of the projectile is low). Therefore, the average displacement of each time step within the last 1000 time steps (accounting for 0.5% of the total time steps), d_{ave}, is used as Δd approximately.

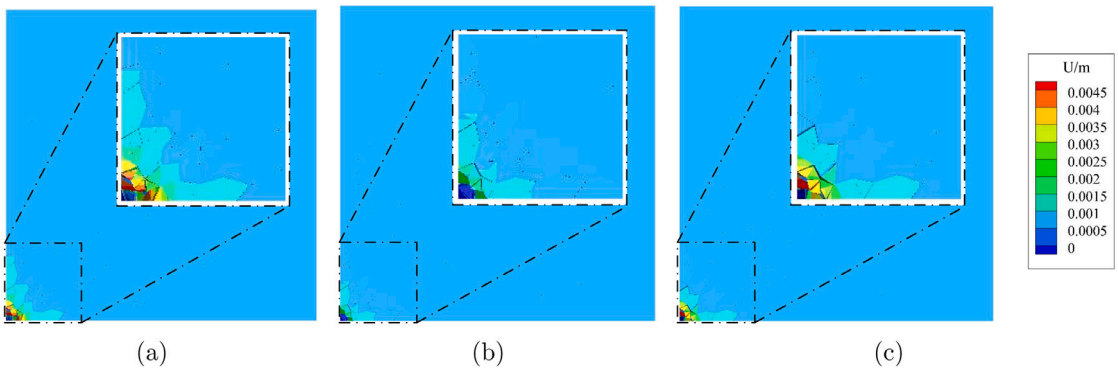

Fig. 15. Craters of (a) plain concrete, (b) 1%FRC and (c) 3%FRC.

A dimensionless number Z is defined as

$$Z = \lceil d_m/\Delta d \rceil, \tag{28}$$

where d_m is the maximum value of all crack surface widths and $\lceil \bullet \rceil$ is the greatest integer function. Z denotes the number of subintervals obtained by dividing the interval $[0, d_m]$ by the approximate length Δd. For convenience, we further modify $\Delta d = d_m/Z$ after Z is obtained. The same values for the maximum crack surface width d_m and minimum fineness Δd are selected for all samples to allow for a direct comparison of the numerical results. According to the numerical results, the maximum widths in all samples are less than or close to a value 1×10^{-4} m; thus, d_m is uniformly taken as 1×10^{-4} m. According to the data shown in Fig. 11, the maximum value of the average displacement d_{ave} is 1.951×10^{-8} m, and we take $\Delta d = 2 \times 10^{-8}$ m. Based on d_m, Δd, and Eq. (28), we can be calculated that $Z = 5000$.

When $Z = 5000$, the interval $[0, d_m]$ is divided into 5000 subintervals with the same length $\Delta d = 2 \times 10^{-8}$ m. The ith subinterval D_i is defined as

$$D_i = \{d | (i-1)\Delta d < d \leqslant i\Delta d,\ i = 1, 2, \ldots, Z\}. \tag{29}$$

All crack surfaces with width d satisfying $d \in D_i$ form a crack surface set G_i:

$$G_i = \{F | d(F) \in D_i,\ i = 1, 2, \ldots, Z\}, \tag{30}$$

where $d(F)$ is the width of crack surface F. Because the length of the subinterval D_i is Δd, and the absolute value of the width difference between any two crack surfaces in the set G_i is less than Δd, the widths of all crack surfaces in this set should be the same according to the definition of Δd. Then, we can take $i\Delta d$ as the unified width d_i of set G_i (the width of any crack surface in G_i is denoted as d_i),

$$d_i = i\Delta d. \tag{31}$$

Furthermore, we define $\tilde{d}_i = d_i/d_m = i/Z$, $i = 1, 2, 3..., Z$, as the normalized crack surface width (abbreviated hereafter as normalized width). Based on Eq. (31), the unified normalized width of the set G_i is $\tilde{d}_i = i/Z$ (the normalized width of any crack surface in G_i is denoted as $\tilde{d}_i$).

Let the number of crack surfaces in set G_i be N_i and the area of the jth$(j = 1, 2, \ldots, N_i)$ crack surface F_i^j be A_i^j (the subscript i indicates that it is contained in set G_i, and the superscript j indicates its serial in G_i). We define the crack surface area A_i of set G_i as the sum of the areas of all crack surfaces in the set:

$$A_i = \sum_{j=1}^{N_i} A_i^j,\ i = 1, 2, \ldots, Z, \tag{32}$$

The normalized crack surface area (abbreviated hereafter as the normalized area) of the set G_i is defined as the ratio of the crack surface area of G_i to the sum of the areas of all the crack surfaces:

$$\tilde{A}_i = \frac{A_i}{A_{tot}}, \tag{33}$$

where A_{tot} is the sum of the areas of all the crack surfaces, which can be written as

$$A_{tot} = \sum_{i=1}^{Z} A_i = \sum_{i=1}^{Z} \sum_{j=1}^{N_i} A_i^j. \tag{34}$$

The values of $\tilde{d}_i$ and $\tilde{A}_i$ are taken as x and y axes, respectively, to draw scatter diagrams. The curves fitted by these scatter diagrams are used to study the relationship between $\tilde{d}_i$ and $\tilde{A}_i$. The distribution of fibers affect the shape of the fitting curves.

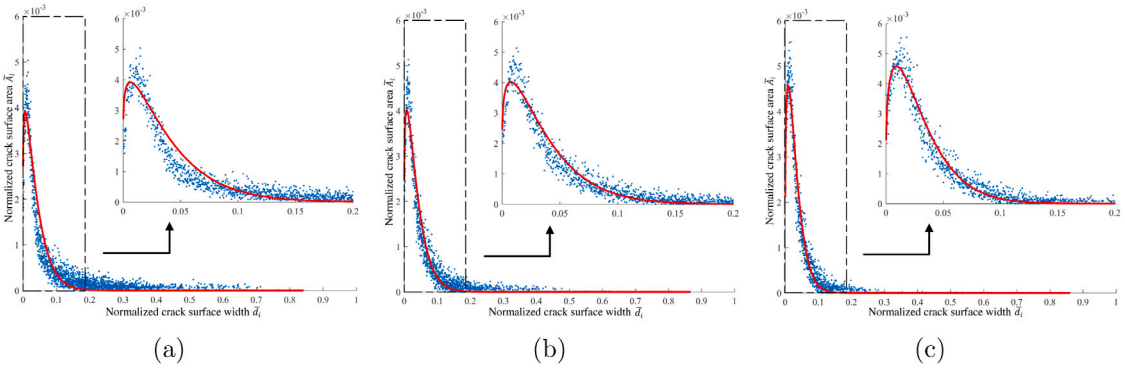

Fig. 16. $\tilde{d} - \tilde{A}$ fitting curves: (a) plain concrete, (b) 1%FRC, (c) 3%FRC.

Table 4
Expectations and variances ($E = \tilde{E}d_m$ with $d_m = 1 \times 10^{-4}$ m).

	Plain concrete	1%FRC	3%FRC
$\tilde{E}$	3.80×10^{-2}	3.59×10^{-2}	3.02×10^{-2}
$\tilde{\sigma}^2$	1.11×10^{-3}	9.35×10^{-4}	5.85×10^{-4}
E	3.80×10^{-6} m	3.59×10^{-6} m	3.02×10^{-6} m

To minimize the influence of randomness and obtain more accurate fitting curves, we simulated ten 1%FRC and 3%FRC samples containing randomly distributed fibers using the same finite element mesh. Then, the 10 normalized areas corresponding to each normalized widths are added and averaged, and three scatter diagrams of $\tilde{d}_i - \tilde{A}_i$ considering statistics are obtained. Finally, according to the probability density function of the Weibull distribution, three $\tilde{d}_i - \tilde{A}_i$ curves are obtained by nonlinear least square fitting. The fitted curves are shown in Fig. 16, and the expectation $\tilde{E}$ and variance $\tilde{\sigma}^2$ are listed in Table 4.

From Fig. 16, we can see that these three curves have similar shapes; all have peaks close to the y axis and drop rapidly on the right side of the peak, gradually tending toward the x axis. In addition, the area between the curve and the x axis is concentrated in the left part of the curve. These results indicate that regardless of the addition of fibers, crack surfaces with smaller widths always account for the majority of all crack surfaces. With an increase in the fiber content, the scattered points become more concentrated, and the width of the band region formed by the scattered points gradually decreases. We can therefore conclude that the addition of fibers can make the crack surface widths more concentrate near the expectation. From the data shown in Table 4, we can see that both the expectation $\tilde{E}$ and variance $\tilde{\sigma}^2$ of the normalized width exhibits a downward trend as fiber content increases. This implies that the expectation of the crack surface width $E = \tilde{E}d_m$ decreases as fiber content increases. That is, an increase in fiber content causes the crack surface widths to be more concentrated around a smaller value.

Let us define $R(z)$ as the sum of the normalized areas A_i of all sets G_i satisfying $i \leqslant z, i = 1, 2, \ldots, Z$,

$$R(z) = \sum_{i=1}^{z} \tilde{A}_i. \tag{35}$$

When $\Delta d \to 0$, $R(z)$ also indicates the area enclosed by the $\tilde{d} - \tilde{A}$ curve, the x axis, the y axis, and a straight line $x = \tilde{d}_z$. According to Fig. 16, the cumulative distribution function (CDF) curve of the normalized width can be obtained by taking the normalized width $\tilde{d}_i$ as the x axis and the accumulated normalized area R as the y axis. These three CDF curves are shown in Fig. 17. When $R = 0.9$, the normalized widths of the plain concrete, 1%FRC, and 3%FRC are 0.1658, 0.1020, and 0.0750, respectively. In other words, for plain concrete, the sum of the areas of the crack surfaces with normalized width less than 0.1658 (the width is less than 1.658×10^{-5} m) accounts for 90% of the total crack surface area. Meanwhile, for 1%FRC and 3%FRC, this value is reduced to 0.1020 (1.020×10^{-5} m) and 0.0750 (7.500×10^{-6} m), respectively. For 1%FRC, this value is 38.5% smaller compared with that of plain concrete; for 3%FRC, this value is 26.5% smaller compared with that of 1%FRC. Taken together, these results indicate that when the fiber content reaches a certain level, the inhibitory effect of fibers on crack initiation and opening will not be significantly enhanced by further increasing fiber content.

5. Conclusion

In this study, a model of projectile penetrating fiber-reinforced concrete is developed based on the continuum discontinuum element method and the fiber-block correlation algorithm. The numerical simulations on the projectile penetrating the plain concrete and the FRC with 1vol% and 3vol% fiber are implemented.

The main conclusions of this study are as follows:

1. The validity of the proposed model is verified by comparing numerical results with experimental data.

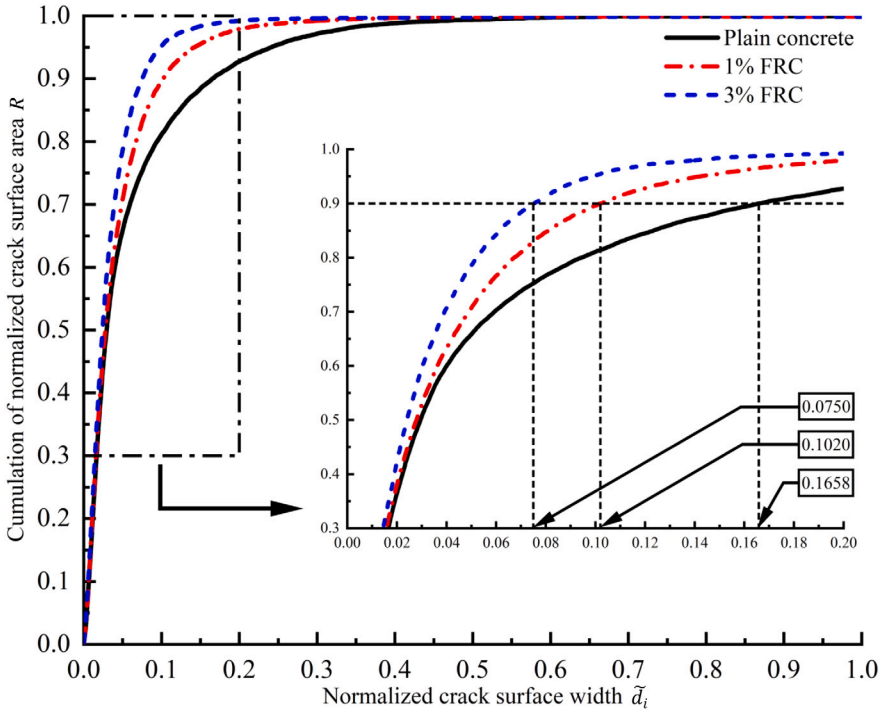

Fig. 17. Cumulative distribution curve of normalized crack surface width.

2. The width-area curve of the crack surface ($\tilde{d}-\tilde{A}$ curve) is consistent with the probability density function curve of the Weibull distribution. In other words, the crack width satisfies the Weibull distribution;

3. Regardless of whether the fibers are added, the crack surfaces with smaller widths are always the majority of all crack surfaces. The addition of fibers reduce the expectation and variance of crack width.

4. Fibers can inhibit the initiation and opening of cracks in concrete; however, this inhibitory effect saturates once fiber content reaches a certain level.

CRediT authorship contribution statement

Bowen Sun: Writing – original draft. **Fei Han:** Writing – original draft. **Chun Feng:** Software, Methodology. **Yong Mei:** Validation, Methodology. **Yunhou Sun:** Investigation. **Jun Shen:** Conceptualization. **Ao Zhang:** Conceptualization.

Declaration of competing interest

The authors declare that they have no known competing financial interests or personal relationships that could have appeared to influence the work reported in this paper.

Data availability

No data was used for the research described in the article.

Acknowledgments

The authors gratefully acknowledge the financial support received from the National Natural Science Foundation (11872016), the Fundamental Research Funds of National Key Laboratory of Shock Wave and Detonation Physics (JCKYS2021212003).

References

[1] Shi CJ, Wu ZM, Xiao JF, Wang DH, Huang ZY, Fang Z. A review on ultra high performance concrete: Part I. Raw materials and mixture design. Constr Build Mater 2015;101:741–51.
[2] Rios JD, Cifuentes H, Leiva C, Seitl S. Analysis of the mechanical and fracture behavior of heated ultra-high-performance fiber-reinforced concrete by X-ray computed tomography. Cem Concr Res 2019;119:77–88.
[3] Yoo DY, Banthia N. Mechanical properties of ultra-high-performance fiber-reinforced concrete: A review. Cem Concr Compos 2016;73:267–80.
[4] Guo Z, Zhuang CL, Li ZH, Chen Y. Mechanical properties of carbon fiber reinforced concrete (CFRC) after exposure to high temperatures. Compos Struct 2021;256:113072.
[5] Ali B, Qureshi LA. Influence of glass fibers on mechanical and durability performance of concrete with recycled aggregates. Constr Build Mater 2019;228:116783.
[6] Zhang JH, Wu ZY, Yu HF, Ma HY, Da B. Mesoscopic modeling approach and application for steel fiber reinforced concrete under dynamic loading: A review. Engineering 2022.
[7] Yoo DY, Banthia N. Mechanical and structural behaviors of ultra-high-performance fiber-reinforced concrete subjected to impact and blast. Constr Build Mater 2017;149:416–31.
[8] Abdallah S, Fan MZ, Rees DWA. Predicting pull-out behaviour of 4D/5D hooked end fibres embedded in normal-high strength concrete. Eng Struct 2018;172:967–80.
[9] Qi JN, Wu ZM, Ma ZJ, Wang JQ. Pullout behavior of straight and hooked-end steel fibers in UHPC matrix with various embedded angles. Constr Build Mater 2018;191:764–74.
[10] Feng J, Sun WW, Wang XM, Shi XY. Mechanical analyses of hooked fiber pullout performance in ultra-high-performance concrete. Constr Build Mater 2014;69:403–10.
[11] Wille K, Kim DJ, Naaman AE. Strain-hardening UHP-FRC with low fiber contents. Mater Struct 2011;44(3):583–98.
[12] Yoo DY, Lee JH, Yoon YS. Effect of fiber content on mechanical and fracture properties of ultra high performance fiber reinforced cementitious composites. Compos Struct 2013;106:742–53.
[13] O' Neil EF, Neeley BD, Cargile JD. Tensile properties of very-high-strength concrete for penetration-resistant structures. Shock Vib 1999;6(5, 6):237–45.
[14] Anderson WF, Watson AJ, Armstrong PJ. Fiber reinforced concretes for the protection of structures against high velocity impact. Struct Impact Crashworthiness 1984;2:687–95.
[15] Máca P, Sovják R, Konvalinka P. Mix design of UHPFRC and its response to projectile impact. Int J Impact Eng 2014;63:158–63.
[16] Wu P, Zhou F, Li QH, Xu SL, Chen BK. Experimental study on the resistance of the ultra high toughness cementitious composites material-fiber concrete composite targets subjected to twice projectiles impact. Explos Shock Waves 2022;42:53–65.
[17] Xiao L, Qu WZ, Wang QJ. Numericai simulation on non-normal penetration into reinforced concrete. In: Applied materials and electronics engineering. 2012.
[18] Shiu W, Donzé FV, Daudeville L. Influence of the reinforcement on penetration and perforation of concrete targets: a discrete element analysis. Eng Comput 2009;26(1/2):29–45.
[19] Heckötter C, Vepsä A. Experimental investigation and numerical analyses of reinforced concrete structures subjected to external missile impact. Prog Nucl Energy 2015;84(6):56–67.
[20] Wang CW, Liu XL, Song DQ, Wang EZ, Zhang JM. Numerical investigation on dynamic response and failure modes of rock slopes with weak interlayers using continuum-discontinuum element method. Front Earth Sci 2021;9:791458.
[21] Ju Y, Liu P, Chen JL, Yang YM, Ranjith PG. CDEM-based analysis of the 3D initiation and propagation of hydrofracturing cracks in heterogeneous glutenites. J Natl Gas Sci Eng 2016;35:614–23.
[22] Zhu XG, Feng C, Cheng PD, Wang XQ, Li SH. A novel three-dimensional hydraulic fracturing model based on continuum–discontinuum element method. Comput Methods Appl Mech Engrg 2021;383:113887.
[23] Feng C, Li SH, Hao WH, Ge W. Numerical simulation on penetrating and blasting process of EPW based on CDEM. J Vib Shock 2017;36(13):11–8.
[24] Wang HZ, Bai CH, Feng C, Xue K, Zhu XG. An efficient CDEM-based method to calculate full-scale fragment field of warhead. Int J Impact Eng 2019;133:103331.
[25] Lin QD, Li SH, Gan YD, Feng C. A strain-rate cohesive fracture model of rocks based on lennard-jones potential. Eng Fract Mech 2022;259:108126.
[26] Feng C, Li SH, Liu XY, Zhang YN. A semi-spring and semi-edge combined contact model in CDEM and its application to analysis of Jiweishan landslide. J Rock Mech Geotech Eng 2014;6(1):26–35.
[27] Li SH, Feng C, Zhou D. Mechanical methods in landslide research. Science Press; 2018.
[28] Jing L, Stephansson O. Fundamentals of discrete element methods for rock engineering. Elsevier; 2007.
[29] Mei Y, Liu JM, Cui Y, Li F, Tang XK, Sun M, Chi RQ, Zhang YB, Zhang A, Chen K. Mechanically excellent nacre-inspired protective steel-concrete composite against hypervelocity impacts. Sci Rep 2021;11(1):1–12.
[30] Han F, Maloth T, Lubineau G, Yaldiz R, Tevtia A. Computational investigation of the morphology, efficiency, and properties of silver nano wires networks in transparent conductive film. Sci Rep 2018;8(1):1–14.
[31] Breitenbücher R, Meschke G, Song FB, Zhan YJ. Experimental, analytical and numerical analysis of the pullout behaviour of steel fibres considering different fibre types, inclinations and concrete strengths. Struct Concr 2014;15(2):126–35.
[32] Feng J, Gao XD, Li JZ, Dong HL, He Q, Liang JG, Sun WW. Penetration resistance of hybrid-fiber-reinforced high-strength concrete under projectile multi-impact. Constr Build Mater 2019;202:341–52.